

Article

# Backscattering Statistics of Labeled Sentinel-1 Wave Mode Imagettes for Ten Geophysical Phenomena

Ziyue Dai <sup>1,2</sup>, Huimin Li <sup>1,2,\*</sup> , Chen Wang <sup>1,2</sup>  and Yijun He <sup>1,2</sup> 

<sup>1</sup> School of Marine Sciences, Nanjing University of Information Science & Technology, Nanjing 210044, China

<sup>2</sup> The Key Laboratory of Space Ocean Remote Sensing and Application, Ministry of Natural Resources, Beijing 100081, China

\* Correspondence: huimin.li@nuist.edu.cn

**Abstract:** Synthetic aperture radar (SAR) is a sensor that is proven to have great potential in observing atmospheric and oceanic phenomena at high-spatial resolutions (~10 m). The statistics of SAR backscattering that describe the image characteristics are essential to help interpret the properties of the geophysical processes. In this study, we took advantage of a hand-labeled database of ten commonly observed geophysical processes created based on the Sentinel-1 wave mode vignettes to document the SAR backscattering statistics. The probability density function (PDF), normalized variance, skewness, and kurtosis were investigated among the ten labeled categories. We found that the NRCS PDFs differ between types, implying the influences of these large-scale features on the radar backscattering distribution. The statistical parameters exhibited distinct variations among classes at the two incidence angles of 23.5° and 36.5°. In particular, the normalized variance of low wind area at 23.5° exceeded other phenomena by an order of magnitude. This lays the basis for directly identifying the SAR images of low wind areas in terms of this parameter. Sea ice and rain cells at 36.5° span within a similar range of kurtosis values, much higher than the other groups. While sea ice could be excluded using a latitude threshold, the rain cells are readily detected. The global percentage map of directly identified rain cells is consistent with the deep-learning results but with higher efficiency. The influence of these large-scale atmospheric and oceanic features on radar backscattering statistics must be considered in the future wave retrieval algorithm for improved accuracy.

**Keywords:** Sentinel-1 wave mode; labeled ten geophysical phenomena; normalized radar cross-section statistics



**Citation:** Dai, Z.; Li, H.; Wang, C.; He, Y. Backscattering Statistics of Labeled Sentinel-1 Wave Mode Imagettes for Ten Geophysical Phenomena. *J. Mar. Sci. Eng.* **2022**, *10*, 1594. <https://doi.org/10.3390/jmse10111594>

Academic Editor: Valery Bondur

Received: 28 August 2022

Accepted: 20 October 2022

Published: 28 October 2022

**Publisher's Note:** MDPI stays neutral with regard to jurisdictional claims in published maps and institutional affiliations.



**Copyright:** © 2022 by the authors. Licensee MDPI, Basel, Switzerland. This article is an open access article distributed under the terms and conditions of the Creative Commons Attribution (CC BY) license (<https://creativecommons.org/licenses/by/4.0/>).

## 1. Introduction

The atmosphere and ocean composed of numerous processes at different scales (from thousands of kilometers to meters) are two significant systems regulating the Earth's weather and climate. Comprehensive measurements are essential to help understand the physics of these processes. In-situ observations, despite their high accuracy, are mostly limited to fixed locations, and are, thus, not suitable for extended spatial coverage. By comparison, spaceborne remote sensing is advantageous in observing atmospheric and oceanic phenomena given its wide coverage across the globe [1]. Among the various satellite sensors, spaceborne synthetic aperture radar (SAR) is now one of the most advanced sensors used to observe sea surface features at high spatial resolution (~10 m). In addition to the commonly observed ocean waves, the phenomena at the km-scale, such as the atmospheric wind streaks, cells, fronts, rivers, etc., are also frequently visible on SAR images [2–9]. In addition to that, SAR is able to acquire observations under all weather conditions during the day and night, making it significant to examine the various geophysical phenomena.

SAR is an active microwave radar and its signal is often characterized by the normalized radar cross-section (NRCS and  $\sigma^0$  used interchangeably hereinafter). The radar return represents the incident energy backscattered to the sensor by the Bragg waves associated with the wind-generated short waves at comparable scales with the radar waves [10]. In reality, long ocean waves are always present on the sea surface, further modulating the

Bragg waves. Such superimpositions of long and Bragg waves lead to the complicated SAR imaging mechanism that includes real aperture radar (RAR) modulation and velocity bunching [11]. The former is composed of tilt modulation (related to the local incidence angle change by the surface slope) and hydrodynamic modulation (long and short wave interaction). The latter is unique to a SAR system, induced by the orbital velocity of the long waves. The modulation acts as a redistribution of the surface backscatter, resulting in a variety of NRCS probability density functions (PDFs). Many models have been proposed to describe the NRCS statistics, including Rayleigh, K, Weibull, log-normal and generalized Gamma distribution, among others [12–16]. The shape parameters are found to vary with the wind speed [17], implying the variety of NRCS distribution under different sea state conditions.

Statistical parameters derived from the moments of SAR NRCS have also been investigated to represent the image properties. The mean and standard deviations, corresponding to the first and second orders of NRCS statistics, are the two mostly explored variables. The average NRCS is usually used to estimate the local wind speed over SAR illuminated scene in terms of the empirical geophysical model function (GMF). A GMF relates the NRCS magnitude to the radar configuration (frequency and incidence angle) as well as the surface wind vectors (speed and direction) [18]. Given the differing levels of radar backscatter, each radar band has its specific GMFs. Among these, the C-band model (CMOD) family is possibly the most popular, originally designated for the C-band scatterometer and later applied to SAR applications as well [19]. Since a SAR has only one antenna and cannot independently resolve the wind direction, an external wind direction is often needed from either collocated observations or model outputs. With the external wind direction, SAR-derived wind speeds have been validated with high accuracy [18,20,21]. Independent wind retrieval has been proposed based on the fully polarimetric SAR measurements [22] and/or introducing the Doppler information in addition to the NRCS [23]. The combination of mean and std, namely, the normalized variance (Nvar) has contributed to the direct estimate of SWH rather than from the inversed wave spectra. Nvar characterizes the relative contrast of radar return over a SAR scene. This parameter is closely related to the local wind conditions as well, exhibiting a monotonic increase [24]. By comparison, the higher order moments variates, such as skewness and kurtosis are less explored. Skewness reflects the asymmetry degree of the NRCS PDF of its mean value. Kurtosis measures the tail length of the NRCS PDF, in other words, the existence of larger radar returns within a SAR scene. Evidence has been found for the departure of kurtosis versus skewness relation from the Rayleigh distribution, implying the contribution from non-Bragg scattering to the radar return [24].

SAR has been shown to have great potential in the examination of many geophysical processes, including both oceanic and atmospheric features [4,7,25]. These phenomena are imaged due to their modulations on the sea surface roughness. For instance, rain cells are often visible on SAR images as circular features with bright outer edges associated with the squall lines. The inner core appears bright or dark depending on the radar frequencies and the rain rate [26]. For C-band SAR, NRCS is found to increase relative to the rain rate for a given sea state and decrease with the sea state [27]. The bright backscattering from rain cells renders the wind retrieval toward a larger wind speed. Another feature captured by SAR images, the low wind area, also has a significant influence on the wind speed inversion, but to the lower end of the realistic conditions [18]. The low wind area, depicted as a dark patch on SAR imagery, is difficult to discern from the crude oil spill of a similar pattern. These widely observed features are mostly investigated in terms of the averaged NRCS, while their impacts on the NRCS distribution or other statistical parameters have not been addressed in detail. In this study, we took advantage of the recently hand-labeled SAR database of ten common geophysical phenomena on SAR images to explore the NRCS statistics, including the NRCS PDF, Nvar, skewness, and kurtosis. The SAR data set is visually selected from the Sentinel-1 wave mode vignettes, composed of two incidence angles ( $23.5^\circ$  and  $36.5^\circ$ ) [25]. The statistical variables were examined for each phenomenon category and compared between the two incidence angles. Applications of Nvar and skewness to distinguish the low wind area

and rain cells are also reported. This paper is organized as follows. Section 2 describes the database and calculation of the statistical variables. The results are presented in Section 3, followed by the Summary in Section 4.

## 2. Data and Method

### 2.1. TenGeoP-SARwv Data Set

Sentinel-1 (S-1) is a satellite constellation composed of two identical SAR sensors (S-1A and S-1B), launched in April 2014 and April 2016, respectively. It is designed to operate at four exclusive imaging modes: extra wide swath (EW), interferometric wide swath (IW), strip map (SM), and wave mode (WV) [28]. Among these, EW and IW primarily focus on the coastal regions in pursuit of extended spatial coverage (400 km for EW and 250 km for IW). To date, SM is seldom activated, only as an experimental mode to sporadically collect acquisitions across the globe. WV is the default mode over the open ocean, acquiring small SAR vignettes of 20 km by 20 km at a spatial resolution of 5 m. WV employs a novel ‘leapfrog’ acquisition pattern that alternately obtains vignettes every 100 km along the satellite track at two incidence angles:  $23.5^\circ$  for WV1 and  $36.5^\circ$  for WV2. The two images at the same incidence angle are 200 km apart. This radar configuration allows examining the SAR imaging sensitivity of the sea surface in terms of incidence angles. Thanks to the powerful sensor hardware, WV is able to continuously collect images across the open ocean, accumulating about 60,000 vignettes per satellite per month. This vast SAR data set is invaluable to atmospheric and oceanographic studies in many aspects. For instance, the push role of ocean waves to sea ice in the Antarctic Ocean has been investigated using S-1 WV acquisitions [29]. A global map of the oil slicks and their sources are examined based on a detailed inventory of more than 560,000 S-1 images [30].

With the drastically increasing volume of S-1 acquisitions, human selections of SAR images of particular features are time-consuming and impractical to extend such studies at the global scale. Automatic data screening has become the primary task to proceed with. Given the significant progress achieved in computer science, the deep learning neural network is now feasible to classify big data. In essence, the neural network is a supervised learning and classification model, which requires a labeled data set as input. To this end, a dedicated S-1 WV database (consisting of 10 commonly observed atmospheric and oceanic phenomena) was established by hand-labeling more than 13,000 images in 2016 [25]. This data set is named TenGeoP-SARwv, representing ten geophysical phenomena frequently visible by S-1 wave mode. It is publicly available at sea scientific open data publication (SEANOE) via <http://www.seanoe.org/data/00456/56796/> (accessed on 10 July 2022). Ten kinds of signatures are included and their short symbols are listed in Table 1 for simplicity in the subsequent analyses. For details on labeling criteria, refer to [25]. Note that only the prevalent signature is tagged on SAR imagery, despite the co-existence of multiple features in some cases. The labeled phenomenon must be homogeneous with clear contrast relative to the background, such as the rain cell and oceanic front just to name a few. Since this study focuses on documenting the statistical parameters among various geophysical phenomena, this data set could not be directly used because all SAR images were recalibrated to sea surface roughness and downsampled to a coarser spatial resolution. Instead, we made use of the original SAR NRCS imagery along with the image tag for each SAR vignette.

All the TenGeoP-SARwv images were obtained at vertically transmitted and vertically received (VV) polarizations and at two incidence angles. Spatial locations of WV1 and WV2 are, respectively, presented in Figure 1a,b to illustrate their global distributions. As shown, the labeled SAR vignettes cover most of the open oceans for both WV1 and WV2. One exception is observed off the European continent in the North Atlantic Ocean, where fewer WV vignettes were collected due to the priority of IW imaging mode for coastal studies. No WV data were acquired proximate to the Arctic Ocean for a similar reason, resulting in the fact that all sea ice cases were scattered around the Antarctic. The number of labeled SAR images per class at the two incidence angles is given at the bottom panel of Figure 1, correspondingly, which presents the uneven distribution of data counts among classes. For WV1, pure ocean swell (denoted by ‘F’) was the most popular class with more than

4000 cases in comparison to the iceberg ('L') of the least count. This was expected since WV1 at 23.5° was more favorable to capture the surface waves due to the strong tilt modulation imaging mechanism. The wind streaks ('G') and micro-convective cells ('H') had 350 and 180 images, less than other classes. It is worth noting that the visibility of one geophysical phenomenon in SAR images relied much on its modulations to the sea surface roughness. As such, the imprint of wind streaks or cells was more easily submerged by the higher backscattered radar signals at WV1, particularly when the phenomenon modulations were weak. This is contrary to the performance of WV2 at 36.5°, which was more sensitive to the sea surface roughness changes. Such sensitivity led to more counts of wind streaks and cells as well as other atmospheric features manifested by WV2, compared to the pure ocean swell, as in Figure 1d. The number of pure ocean swells was less than 500 vignettes, due to the fact that one or more geophysical signatures often co-existed on most of these WV2 images. TenGeoP-SARwv took the prevalent feature as the tag and multiple labeling were not implemented at this stage. In other words, the pure ocean swell was usually overlapped with another kind of phenomenon but was less dominant. Despite the data count not being uniformly distributed across classes, the number of labeled images was readily sufficient for the deep learning classification, as demonstrated in [31].

**Table 1.** Ten labeled phenomena and their short symbols in this study.

Phenomenon	Symbol	Phenomenon	Symbol
Pure ocean swell	F	Wind streaks	G
Micro-convective cells	H	Rain cells	I
Biological slicks	J	Sea ice	K
Iceberg	L	Low wind area	M
Atmospheric front	N	Oceanic front	O

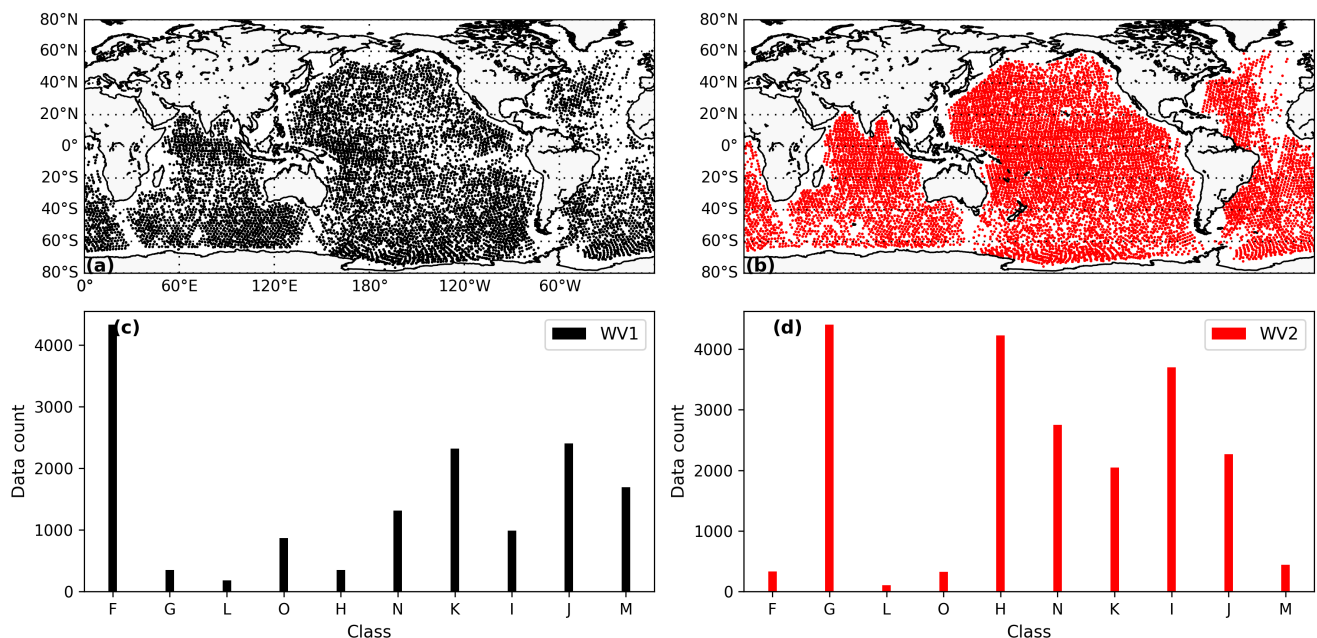


**Figure 1.** Global distribution of the TenGeoP-SARwv data set for all classes at (a) WV1 and (b) WV2. Individual data counts of labeled SAR images for each class at (c) WV1 and (d) WV2. Symbols corresponding to each class are referred to in Table 1.

2.2. Parameter Calculation

For S-1 WV, there are usually 5000 by 5000 px along the radar range and azimuth directions over one SAR vignette. The mean and standard deviations of NRCS are the

two parameters mostly used to describe the image statistics. From a statistical point of view, they represent the first- and second-order moments of the radar return, respectively. The combination of these two variables, known as the normalized variance (Nvar), is defined by

$$Nvar = \frac{\sigma^2}{\mu^2} \tag{1}$$

where  $\sigma$  denotes the standard deviation of NRCS and  $\mu$  is the mean. Figure 2a presents the Nvar distribution calculated at the original pixel spacing for both WV1 and WV2. It is clear that the Nvar PDF was distinct between these two incidence angles, with WV1 spanning a wider extent than WV2. WV1 Nvar was quasi-uniformly distributed in the range of [1.4, 2.0] with a mean of 1.81, while WV2 Nvar was tightly concentrated around 1.2. Such a difference implies that the NRCS variability extent (relative to the mean) was more consistent for WV2 than WV1. Yet, it should be noted that  $\sigma$  (over one imagery) varied with the spatial resolution. When the pixel resolution became coarser (increasing the number of averaged pixels), the Nvar constantly decreased for both WV1 and WV2. This Nvar variation with the number of averaged pixels is illustrated in Figure 2b. The change was in a logarithmic order as depicted by the regression curves. Since we tend to document the influences of the large-scale features on these NRSC statistical parameters, all SAR images were processed by an averaging box that moved every 10 px. This resulted in a 10th value roughly of the Nvar at the original resolution. This downsampling procedure is adopted in the subsequent analyses unless otherwise stated.

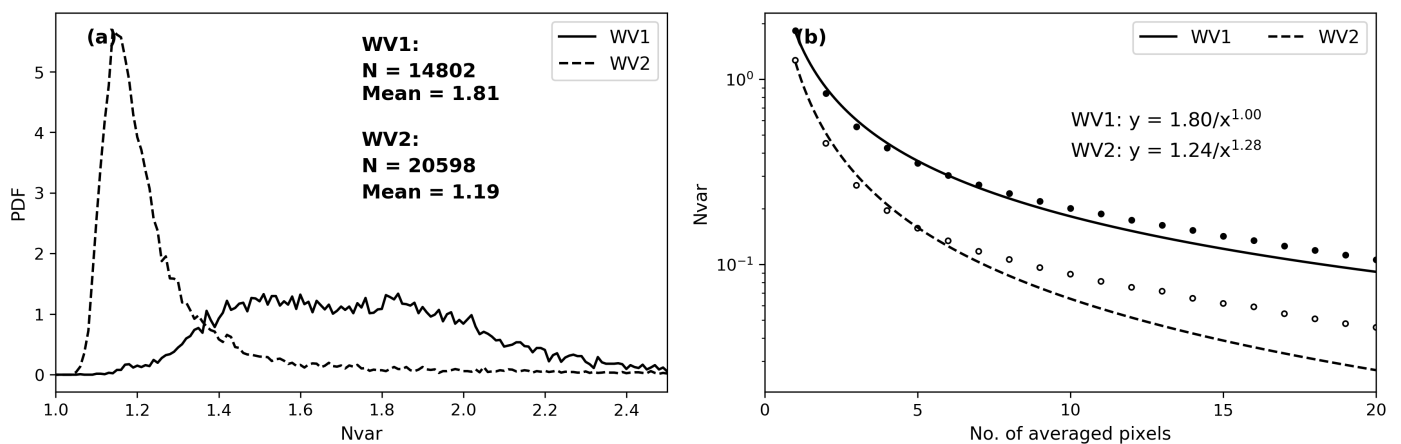


**Figure 2.** (a) PDF of Nvar at the original pixel resolution. (b) Variation of Nvar relative to the number of averaged pixels. The scatter was calculated based on a SAR case example; the curves are the regression lines with the mathematical format annotated in the plot.

The higher-order moments of radar returns are also very useful to describe the NRCS characteristics in addition to the mean and standard deviations. The NRCS PDF is expected to follow a Rayleigh distribution based on theories; however, in reality, very few SAR images show this distribution. It is partially attributed to the contribution of non-Bragg scattering associated with the surface wave breaking [24]. There is a need to describe the higher-order NRCS features, and skewness and kurtosis are practical to such an end. They are defined as

$$skewness = \frac{m_{3c}}{\sigma^3} \tag{2}$$

and

$$kurtosis = \frac{m_{4c}}{\sigma^4} \tag{3}$$

where  $m_{ic}$  is the  $i$ th-order centered moment and  $\sigma$  is the standard deviation. In terms of the statistics theory, skewness measures the degree of asymmetry of the NRCS PDF relative to its mean value. The NRCS PDF roughly tends to exhibit a long tail on the right side of the

mean value, corresponding to a positive skewness. SAR cases of negative skewness also exist, particularly at larger incidence angles. Kurtosis is widely employed to describe the tailedness of a PDF. In other words, a higher kurtosis corresponds to a greater chance of outliers. Both skewness and kurtosis are simplified yet useful measures of the PDF shape, without direct examination of the PDF itself per se.

### 3. Results and Discussions

In this section, the behaviors of the three statistical parameters are presented and discussed, along with their global distributions. Applications using the selected parameters (to directly distinguish the class of rain cells and low wind areas) are also demonstrated, respectively.

#### 3.1. Statistics of TenGeoP-SAR $wv$

Most of the previous studies examined the NRCS PDFs by taking all of the image features as an ensemble without distinguishing the geophysical phenomena [14,32,33]. NRCS PDFs were distinct between different categories for both WV1 and WV2, as presented in Figure 3. Taking the pure ocean swell as a reference, given that it was the most basic feature on the ocean surface, some phenomena were nearly consistent with this reference while others showed deviations. For WV1 in Figure 3a, the ten phenomena could be divided into four groups. Among these, the wind streaks, icebergs, and atmospheric fronts showed similar NRCS distributions compared to the pure ocean swell. Their PDFs covered a wide range of NRCS values from 0.1 to 0.6 in linear units. Oceanic front and rain cells belonged to a similar group whose mean NRCS was slightly lower, around 0.15. In comparison to the swell group, the low backscattering of these two features accounted for a larger portion. This was expected since the low to medium winds were actually favorable for SAR imaging of the oceanic front and rain cells while high winds tended to blur these two phenomena [31]. The third group consisted of micro-convective cells, biological slicks, and sea ice with their NRCS PDFs shifting toward the smaller values. These three signatures are often visible as dark patterns on SAR images, which are mostly captured under relatively low wind conditions. The downdraft associated with the micro-convective cells suppresses the sea surface roughness, causing low backscattering compared to the updraft with enhanced surface roughness. For a similar reason, biological slicks of reduced roughness also exhibit dark features than the surroundings. The fourth group, the low wind area plotted in the inner axis, was quite different from the other nine phenomena, whose NRCS PDF showed a monotonic decrease. As defined in [25], the low wind area covered an extended region of the low radar return, resulting in a drastically high PDF at a small NRCS.

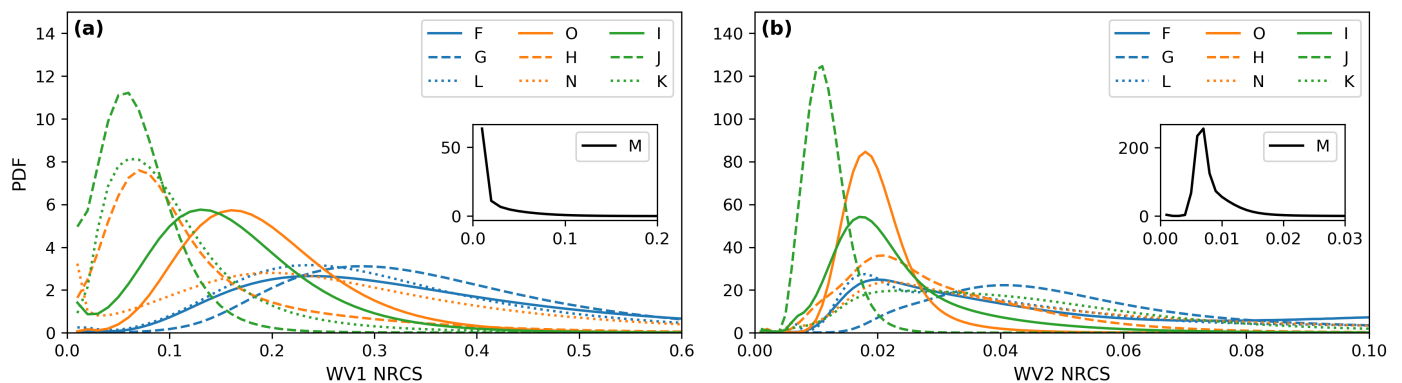


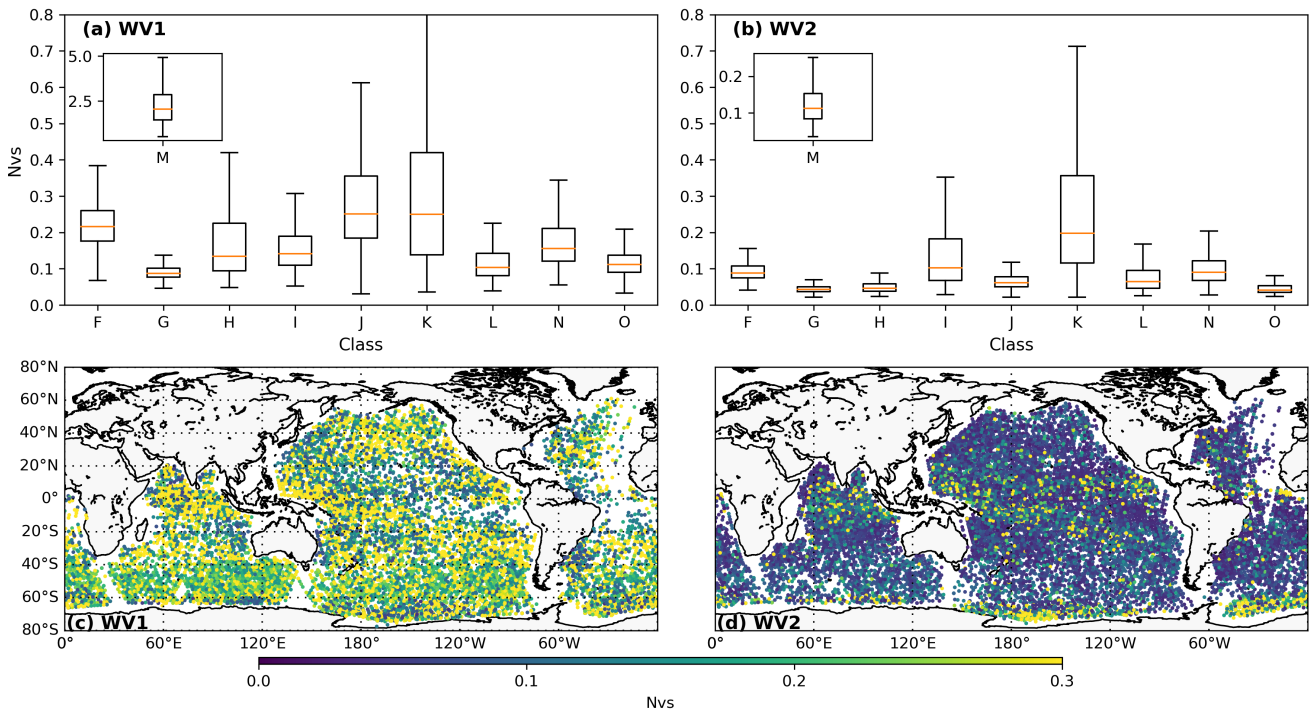
Figure 3. NRCS PDFs of the ten labeled classes for (a) WV1 and (b) WV2.

Figure 3b shows the average NRCS PDF of the labeled classes for WV2. These ten classes of WV2 can only be divided into three groups. Six classes, including micro-convective cells, sea ice, icebergs, atmospheric front, oceanic front, and rain cells, resemble

the NRCS PDF of the pure ocean swell, with variant PDF widths. In particular, the NRCS PDFs of the oceanic front and rain cells were much narrower than the others, consistent with the behavior of WV1. The wind streaks showed larger mean NRCS and wider distributions, possibly due to the higher sensitivity of radar backscattering at  $36.5^\circ$  to the surface roughness modulation by the wind streaks. The other two classes of biological slicks and low wind areas had similar NRCS PDFs, with lower mean values of around 0.08 in linear units. It should be pointed out that discrepancy indeed existed between WV1 and WV2 as shown in Figure 3a,b, which might have resulted from the differing surface scattering mechanisms at these two incidence angles. For WV1 at  $23.5^\circ$ , specular scattering still made a significant contribution to the total radar return, while Bragg scattering was prevalent at WV2. The weaker sensitivity of radar backscattering to the change of surface roughness at WV1 was also a factor influencing the image representation of these large-scale features. These reasons might result in a distinct NRCS PDF for a given class.

Though NRCS PDFs specify the range of backscattering values over a SAR scene, they are not straightforward enough to compare among a vast SAR image data set. Instead, the statistical parameters (as defined above) are more convenient for demonstrating the resemblance and differences between classes. Figure 4 shows the box plots of Nvar for both WV1 and WV2 as well as their global map. Note that Nvar values presented here were calculated based on the downsampled SAR images rather than at the original resolutions, leading to much smaller Nvar values than those shown in Figure 2a. WV1 Nvar was distributed within the range of [0.1, 0.4] for most of the classes. The low wind area at WV1 annotated in the inner axes exhibited the largest extent and its Nvar value was dramatically higher than the other classes. Such a feature made it feasible to be directly used for discerning the low wind area, which will be demonstrated later in the next subsection. In general, the Nvar was more loosely distributed at WV1 than at WV2, implying the various degree of modulation depths to the radar return by these large-scale phenomena at smaller incidence angles. For WV2, the Nvar of wind streaks, micro-convective cells, biological slicks, and the oceanic front were all tightly distributed, while the sea ice spanned a wider extent. Yet, the ten classes for WV2 were all within a similar range, making it difficult to distinguish one particular phenomenon, similar to how the low wind area at WV1 does. The global pattern of Nvar in the bottom panel of Figure 4 is similar between WV1 and WV2, with a larger magnitude at WV1. As shown, Nvar in the tropics is relatively higher than in the extratropics. Across the boundary between the trade winds and westerlies, Nvar reaches the minimum values. Southward of the  $60^\circ$  S, where the sea ice cases are located, the largest Nvar at WV2 was observed, corresponding to the higher box plot in Figure 4b. The maximum Nvar at WV2 was found in the coastal regions of the main continents, possibly induced by the low wind area.

The box plot of skewness is plotted in Figure 5 for WV1 and WV2, along with their global map. For WV1, 99.47% of the SAR cases showed positive skewness, while the negatively skewed SAR images were mostly distributed among sea ice and icebergs. In terms of the skewness magnitude, the sea ice and low wind area exceeded other classes. Their third quartile reached up to 3.0, while the others were mostly below 1.5, as in Figure 5a. For WV2, the positively skewed cases accounted for 97.18%, slightly lower than that of WV1. All ten classes included cases of negative skewness. Sea ice, rain cells, and the iceberg spanned a wider range than the other classes with a much higher third quartile. These three classes consisted of a greater variety of skewness, possibly due to the diverse impacts of these geophysical processes on the NRCS PDF. The skewness of the other categories showed relatively tighter distributions within a narrower extent, in other words, their influence on the NRCS PDF resembled each other. No class stood out compared to the Nvar of the low wind area for WV1, meaning that this parameter is not suitable for directly distinguishing one particular phenomenon at WV2. The global map of the skewness shown in the bottom panel of Figure 5 depicts similar patterns to the Nvar in Figure 4. Higher skewness is observed in the trade winds and polar regions around the Antarctic, typical of locations of the rain cells and sea ice.



**Figure 4.** (Top) box plot of Nvar for the ten labeled classes at (a) WV1 and (b) WV2. (Bottom) global map of the labeled Nvar at (c) WV1 and (d) WV2.

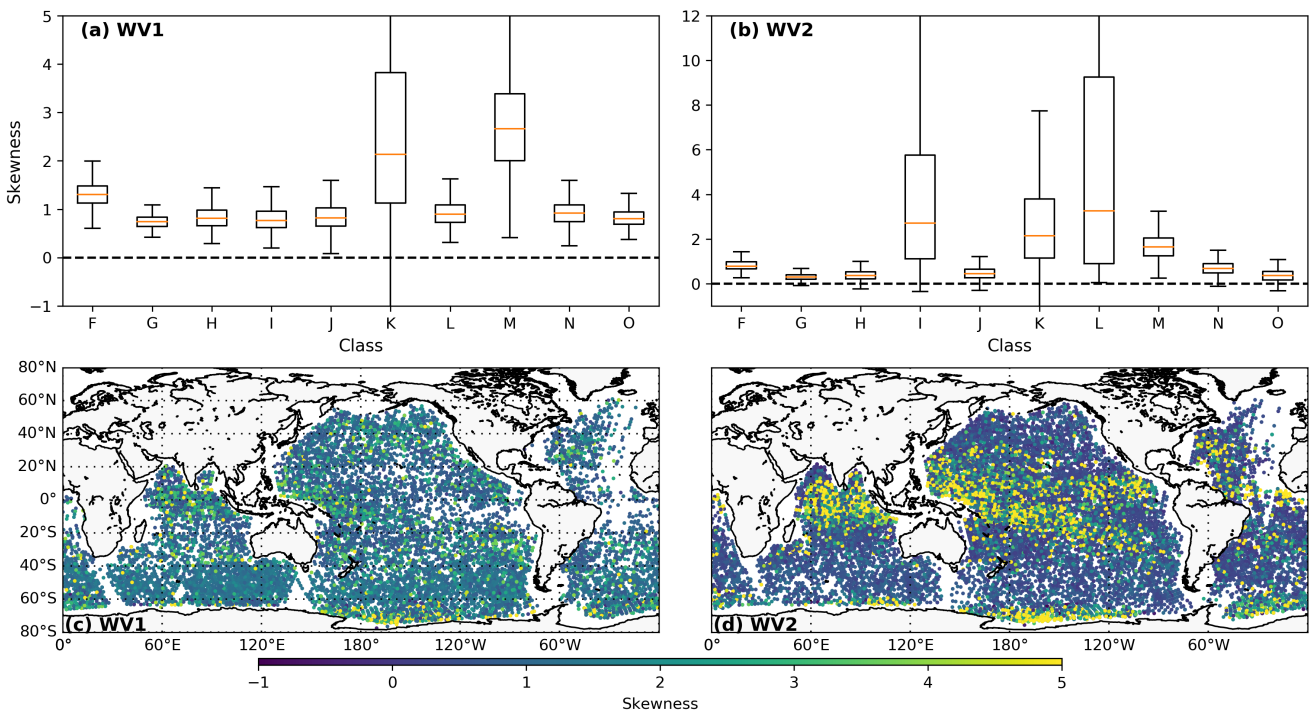


**Figure 5.** The same as in Figure 4 but for the skewness.

Kurtosis, similar to skewness, describes the shape of a PDF by characterizing the tailedness of the NRCS distribution. Higher kurtosis corresponds to a greater proportion of outliers relative to its mean NRCS. Figure 6 gives the box plot of kurtosis for each class as well as the global map. For WV1 in Figure 6a, the kurtosis of most of the classes (except sea ice and low wind area) was lower than the value of 10. The third quartile was generally below 5 and the first quartile was around 2, suggesting a tight distribution of kurtosis.

Such a feature implies that the extremely high backscattering accounts for a very small portion of these classes. By contrast, kurtosis of the sea ice and low wind area covered a wider range and exceeded other classes. Bright NRCS not only existed on these SAR images but showed variant signatures from one case to another. Kurtosis of sea ice at WV2 was comparable to that of WV1, spanning a wider range and outnumbering other classes. A notable difference between WV1 and WV2 is that the kurtosis of rain cells and icebergs stand out; the low wind area exhibited similar features to the pure ocean swell. WV2 at 36.5° is more sensitive to the iceberg visible as bright targets on a SAR scene, inducing such extremely high kurtosis even compared to the class of sea ice and rain cells. This high kurtosis of iceberg makes it distinguishable from the rain cells given that the sea ice could be excluded using the latitude threshold. The global map of kurtosis shown in the bottom panel of Figure 6 resembles the spatial patterns of both Nvar and skewness. Kurtosis was generally high south of the 60° S due to the sea ice class and over the trade winds due to the rain cells.

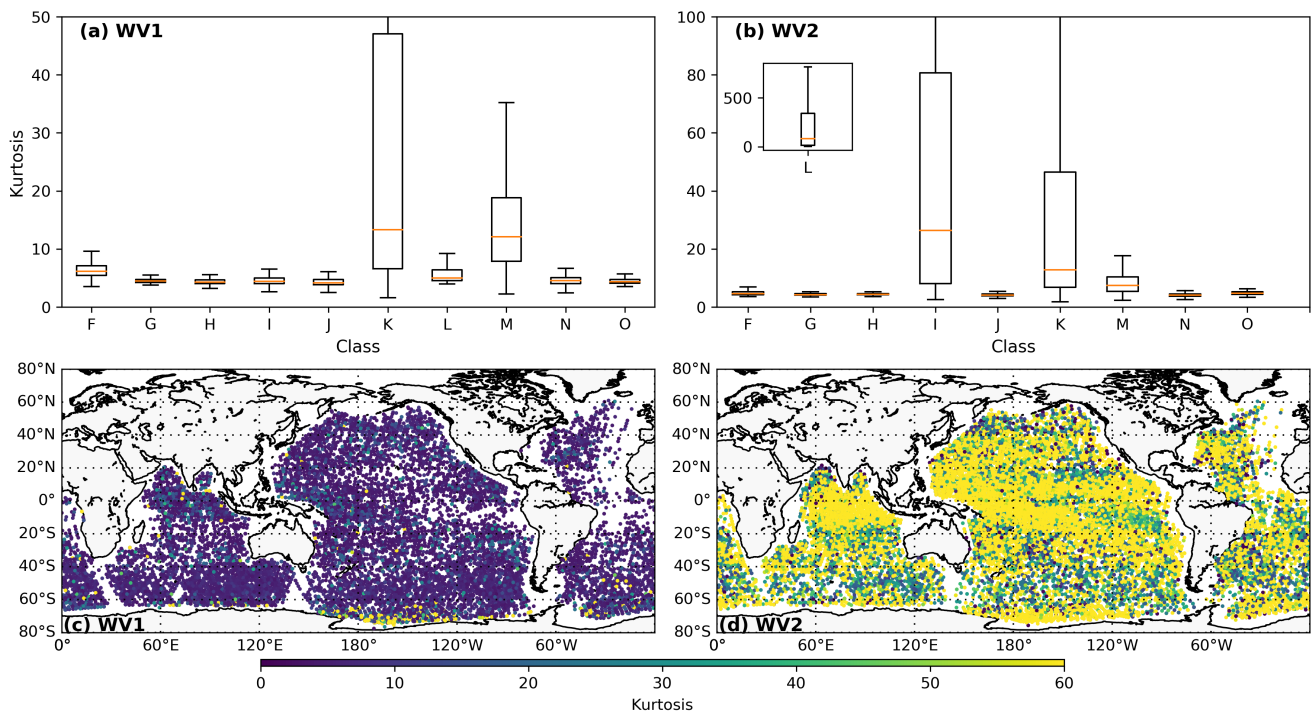


Figure 6. The same as in Figure 4 but for the kurtosis.

### 3.2. Detection of Rain Cells and Low Wind Area

The three statistical parameters presented above characterize the shapes of NRCS PDFs over the ten labeled geophysical phenomena. The similarities and dissimilarities among these ten classes lay the basis for directly using one variable to distinguish a particular phenomenon. For instance, the Nvar of the low wind area at WV1 exhibited much higher values compared to the other class, which could be readily used to filter out these cases. In addition, the kurtosis of rain cells was also notable given the sea ice and iceberg classes could be excluded by a latitude threshold. Such an application is demonstrated in the following based on these two variables for rain cells and low wind area detection.

Figure 7a illustrates a SAR image example of rain cells acquired by S-1A WV2. The collocated European Center for Medium-range Weather Forecast (ECMWF) wind speed was  $4.3 \text{ m s}^{-1}$ , under low wind conditions, suitable to image the rain cells. Two areas of interest marked by the rectangles in colors were selected, one includes the homogeneous signature of ocean waves and the other is over clear rain cells. The circular feature encircles a bright patch, induced by the enhanced sea surface roughness associated with the rain droplets. Note that the dark pattern in the north of the bright feature is possibly due to the damped

waves by the rain. The NRCS PDF shown in Figure 7b is distinct between the ocean waves and the rain cells. The curve of the rain cells area had a higher and longer tail at larger backscattering than the ocean waves. This resulted in a large kurtosis over the entire SAR scene, despite the relatively low kurtosis over the two individual areas of interest. Based on this, a simple criterion of kurtosis lying within the range of [15, 55] is employed to filter out the rain cell cases at WV2. The global percentage map of the detected rain cells using this criterion is presented in Figure 7c. As expected, the rain bands beside the equator had a relatively greater chance of capturing the rain cells above 15%, consistent with the results reported in [31]. It is also worth noting that high wind conditions did not favor the detection of SAR cases with rain cells. This corresponds to the low detection percentage in the extratropics of the Southern Hemisphere, where the winds are constantly high throughout the year.

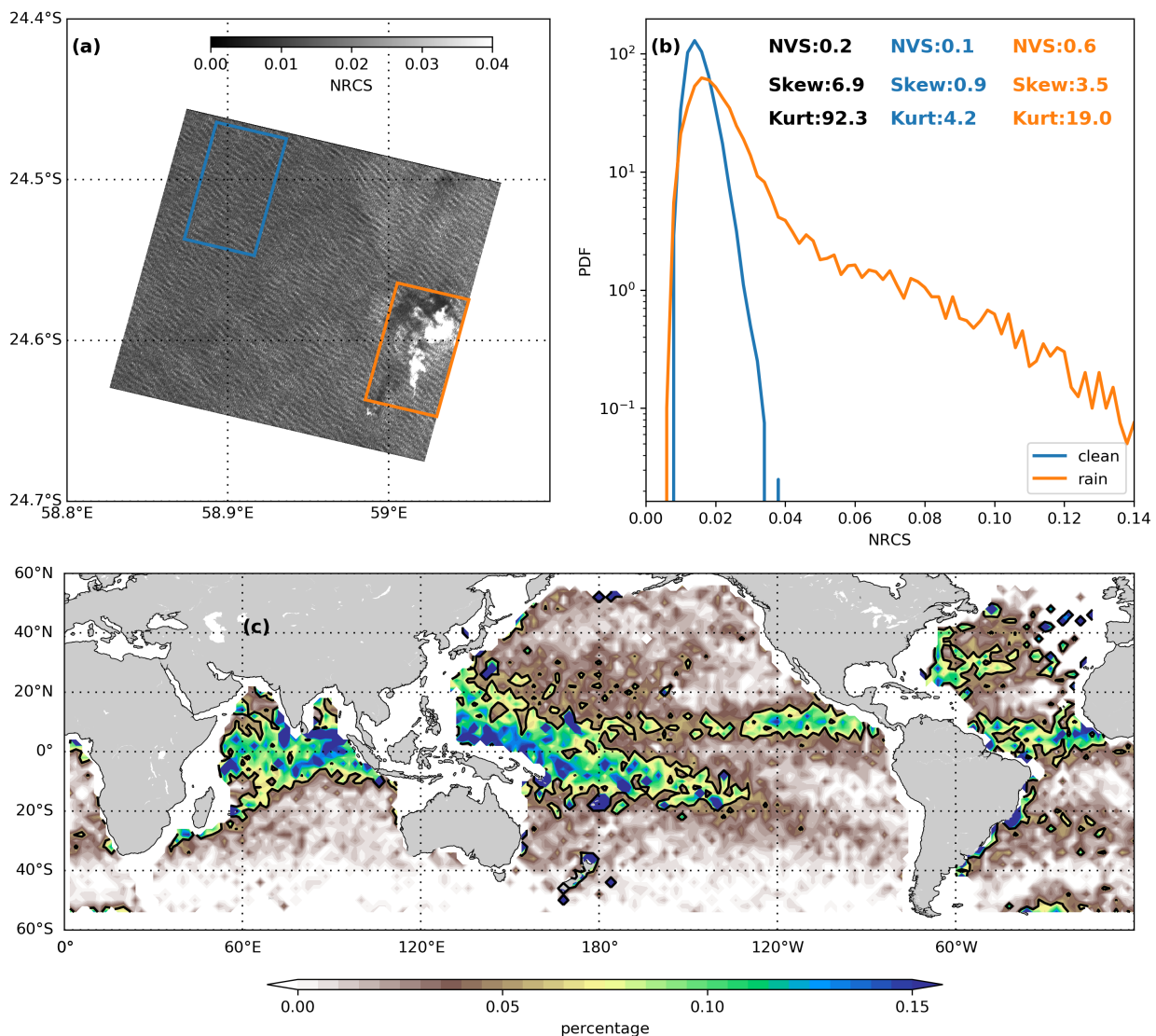


**Figure 7.** (a) A SAR NRCS image labeled as rain cells acquired by WV2; (b) the NRCS PDFs over the area of interest marked by the rectangles in colors as well as the entire SAR image (black curve). The three statistical parameters are accordingly annotated in the plots. (c) The global percentage map of the detected rain cells based on the kurtosis criteria for WV2.

Given the distinct feature of Nvar for the low wind area class at WV1 shown in Figure 4a, it is worthwhile to explore the potential of using Nvar to directly screen these cases for the dedicated applications. Figure 8 presents a case of the low wind area and the

global percentage map detected using Nvar criteria. The low wind area is often visible as an extended dark patch on the SAR image as in Figure 8a. Such a feature is often similar to the crude oil spill and could be readily discerned with the help of extra information [34]. In this case, low winds co-existed with clear ocean wave signatures in the bottom-left corner of the SAR image. The NRCS PDFs in Figure 8b evidence the low backscattering over the low wind area marked by the blue rectangle in Figure 8a. The high contrast of radar return between ocean waves and low winds caused a relatively higher standard deviation, further yielding the larger Nvar as annotated. To directly recognize the SAR cases with low wind area features, a simple Nvar threshold was employed of Nvar, larger than 0.8. The percentage map at a bin of 2° by 2° on the global scale is shown in Figure 8c. Low winds are mostly distributed in the coastal regions, such as southeast Asia and the east coast of America. Its occurrence on the North Indian Ocean is also notable with a percentage higher than 5%, which might correspond to the low wind conditions during the dry seasons. In the extratropics of the Southern Hemisphere, the winds are consistently high, leading to rare detection of low winds below 0.5%. These filtered low-wind cases could be readily used for further analyses without the need for complicated classification models.

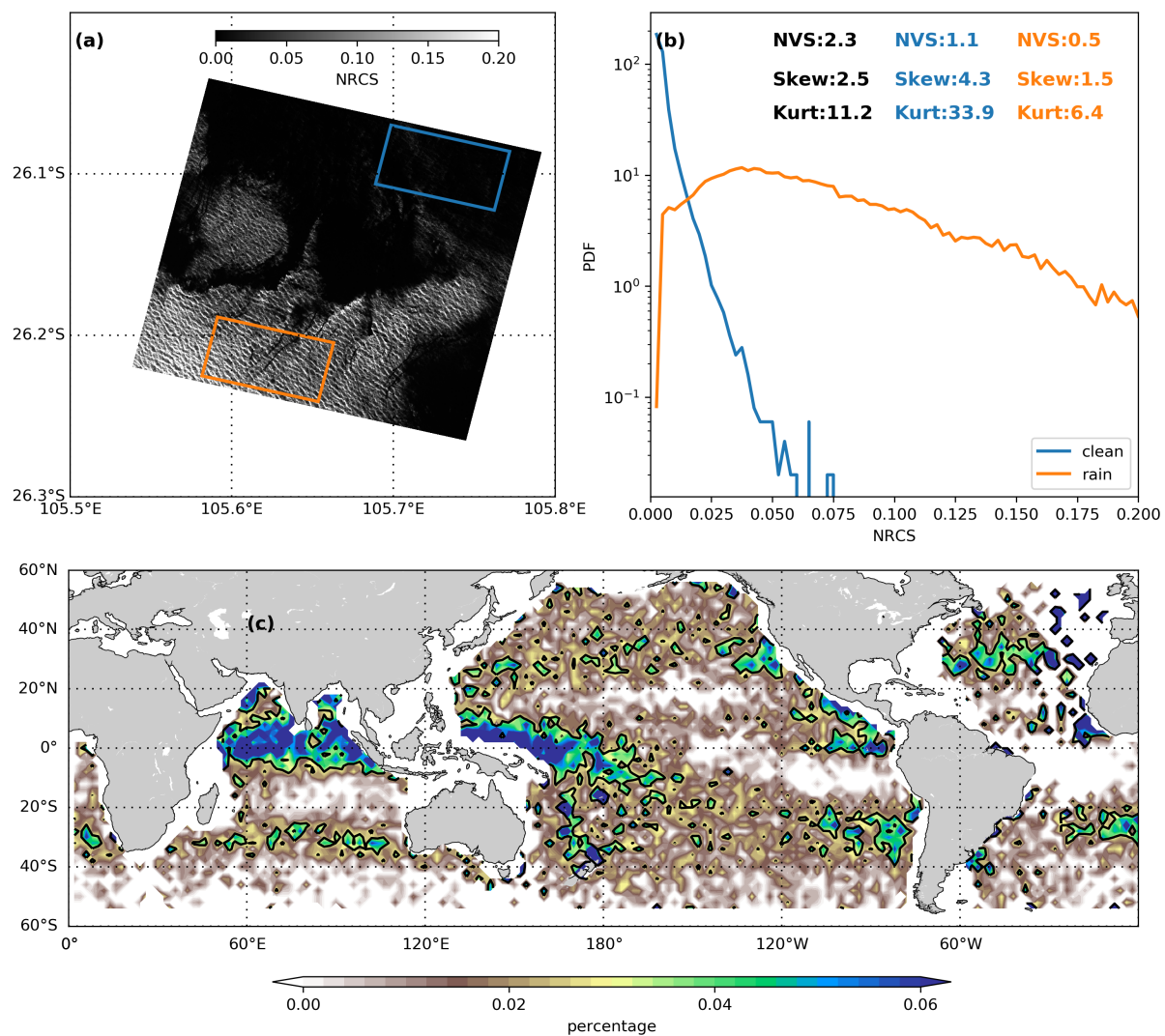


**Figure 8.** (a) A SAR NRCS image of a low wind area at WV1; (b) the NRCS PDFs over the area of interest marked by the rectangles in colors as well as the entire SAR image (black curve). The three statistical parameters are accordingly annotated in the plots. (c) Global percentage map of the detected low wind area using the Nvar-based criteria for WV1.

To demonstrate the practicality of the above-proposed filtering criteria for rain cells and low-wind area detection, these criteria were systematically applied to the S-1A WV images acquired between January 2015 and December 2017. In total, there were about 1.5 million SAR vignettes accumulated at two incidence angles. Note that the low wind area detection was carried out for WV1 at the  $23.5^\circ$  incidence, while the rain cells for WV2 were at a  $36.5^\circ$  incidence. Figure 9 presents the individual percentage map of the detected rain cells and low wind area at a bin of  $2^\circ$  for both latitude and longitude. One can clearly see that the spatial patterns of both percentage maps were essentially similar to those of the maps produced based on the curated data set in Figures 7 and 8. Rain cells in the top panel were primarily located in the rain bands of the tropics with rare detection in the southern extratropics. Yet it should be pointed out the detected percentage using the whole SAR database was smaller than that of the labeled data set. This is due to the fact that the labeling process tried to equalize the number of SAR images among the ten categories, leading to the overestimation of the detected percentage. SAR images of rain cells were roughly overestimated by 5% based on the whole SAR data set. In other words, the hand-labeled data set was not introduced to certain degree biases in the detected proportion. Most of the low wind areas were also observed in the tropical Indian Ocean and off Southeast Asia.

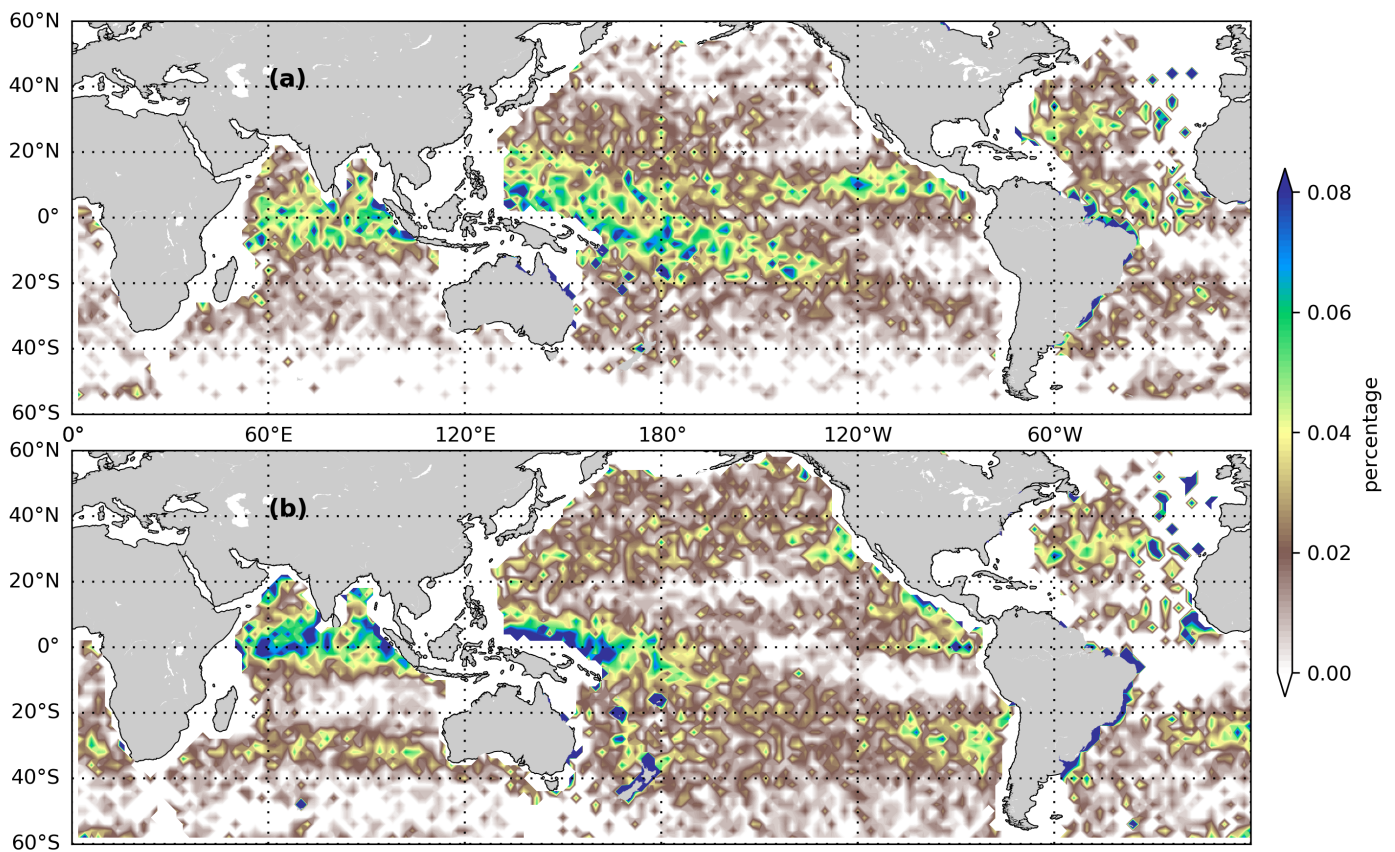


**Figure 9.** Global percentage map of detected SAR images with (a) rain cells and (b) low wind area based on the above-defined detection criteria using S-1A WV acquisitions from January 2015 to December 2017.

#### 4. Summary

SAR is recognized as one of the most potential sensors for observations of atmospheric and oceanic phenomena at the global scale given its high spatial resolution and consistent data sampling. Thanks to the dramatic progress in satellite hardware, continuous SAR acquisitions over the open ocean are now feasible, accumulating a huge SAR database to explore. Ten commonly observed atmospheric and oceanic phenomena have been selected to construct a hand-labeled data set in [25]. Based on this, statistics of the normalized

variance, skewness, and kurtosis of these SAR vignettes are analyzed in this paper. Some of the classes are distinct, for instance, the low wind area shows a much larger Nvar at WV1 and the kurtosis of rain cells exceeds the others. Global patterns of these three statistical parameters are similar, with high values in the tropics as well as around the Antarctic where the sea ice is distributed. Direct screening of low winds and rain cells based on one single parameter is also demonstrated and analyzed with consistent spatial patterns as shown in the previous studies. Such a test makes it possible to extract these cases from the vast SAR database using the proposed criteria, which is expected to simplify the selection process of these two particular phenomena. Results obtained in this study shall particularly facilitate dedicated efforts on regional or global analyses of low winds and rain cells. In addition, the impact of these large-scale features on NRCS PDFs is evident, possibly yielding an influence on the wave retrieval from SAR measurements. Yet the current SAR wave retrieval algorithm has not taken this aspect into account, which should be addressed in the future to improve retrieval accuracy.

**Author Contributions:** Conceptualization, H.L. and C.W.; methodology, H.L.; formal analysis, Z.D.; investigation, Z.D. and H.L.; writing—original draft preparation, Z.D. and H.L.; writing—review and editing, H.L., C.W., and Y.H.; supervision, Y.H.; funding acquisition, Y.H. All authors have read and agreed to the published version of the manuscript.

**Funding:** This work was supported by the National Natural Science Foundation of China under grants 42006163 and 42027805, the Natural Science Foundation of Jiangsu Province under grant BK20210666.

**Data Availability Statement:** The TenGeoP-SARwv data set is publicly available on SEANOE via <https://doi.org/10.17882/56796> accessed on 27 August 2022.

**Acknowledgments:** Copernicus Sentinel data (2016, 2017) were used. The ECMWF forecast winds were obtained in the framework of the Sentinel-1 A Mission Performance Center and are publicly available ([www.ecmwf.int](http://www.ecmwf.int) accessed on 10 July 2022).

**Conflicts of Interest:** The authors declare no conflict of interest.

## References

1. Shutler, J.D.; Quartly, G.D.; Donlon, C.J.; Sathyendranath, S.; Platt, T.; Chapron, B.; Johannessen, J.A.; Girard-Ardhuin, F.; Nightingale, P.D.; Woolf, D.K.; et al. Progress in satellite remote sensing for studying physical processes at the ocean surface and its borders with the atmosphere and sea ice. *Prog. Phys. Geogr. Earth Environ.* **2016**, *40*, 215–246. [[CrossRef](#)]
2. Levy, G. Boundary layer roll statistics from SAR. *Geophys. Res. Lett.* **2001**, *28*, 1993–1995. [[CrossRef](#)]
3. Ufermann, S.; Romeiser, R. Numerical study on signatures of atmospheric convective cells in radar images of the ocean. *J. Geophys. Res. Ocean.* **1999**, *104*, 25707–25719. [[CrossRef](#)]
4. Johannessen, J.A.; Shuchman, R.A.; Digranes, G.; Lyzenga, D.R.; Wackerman, C.; Johannessen, O.M.; Vachon, P.W. Coastal ocean fronts and eddies imaged with ERS 1 synthetic aperture radar. *J. Geophys. Res. Ocean.* **1996**, *101*, 6651–6667. [[CrossRef](#)]
5. Espedal, H.A.; Johannessen, O.M.; Knulst, J. Satellite detection of natural films on the ocean surface. *Geophys. Res. Lett.* **1996**, *23*, 3151–3154. [[CrossRef](#)]
6. Young, G.S.; Sikora, T.N.; Winstead, N.S. Use of Synthetic Aperture Radar in Finescale Surface Analysis of Synoptic-Scale Fronts at Sea. *Weather Forecast.* **2005**, *20*, 311–327. [[CrossRef](#)]
7. Alpers, W.; Zhang, B.; Mouche, A.; Zeng, K.; Chan, P.W. Rain footprints on C-band synthetic aperture radar images of the ocean—Revisited. *Remote Sens. Environ.* **2016**, *187*, 169–185. [[CrossRef](#)]
8. Ahmad, W.; Kim, D. Estimation of flow in various sizes of streams using the Sentinel-1 Synthetic Aperture Radar (SAR) data in Han River Basin, Korea. *Int. J. Appl. Earth Obs. Geoinf.* **2019**, *83*, 101930. [[CrossRef](#)]
9. de Roda Husman, S.; van der Sanden, J.J.; Lhermitte, S.; Eleveld, M.A. Integrating intensity and context for improved supervised river ice classification from dual-pol Sentinel-1 SAR data. *Int. J. Appl. Earth Obs. Geoinf.* **2021**, *101*, 102359. [[CrossRef](#)]
10. Hasselmann, K.; Raney, R.K.; Plant, W.J.; Alpers, W.; Shuchman, R.A.; Lyzenga, D.R.; Rufenach, C.L.; Tucker, M.J. Theory of synthetic aperture radar ocean imaging: A MARSEN view. *J. Geophys. Res. Ocean.* **1985**, *90*, 4659–4686. [[CrossRef](#)]
11. Alpers, W.R.; Ross, D.B.; Rufenach, C.L. On the detectability of ocean surface waves by real and synthetic aperture radar. *J. Geophys. Res. Ocean.* **1981**, *86*, 6481–6498. [[CrossRef](#)]
12. Kuruoglu, E.; Zerubia, J. Modeling SAR Images with a Generalization of the Rayleigh Distribution. *IEEE Trans. Image Process.* **2004**, *13*, 527–533. [[CrossRef](#)] [[PubMed](#)]

13. Pastina, D.; Lombardo, P.; Bucciarelli, T. Statistical analysis of multipolarisation/multifrequency SAR images of the sea surface. In Proceedings of the IGARSS 2000—IEEE 2000 International Geoscience and Remote Sensing Symposium—Taking the Pulse of the Planet: The Role of Remote Sensing in Managing the Environment—Proceedings (Cat. No.00CH37120), Honolulu, HI, USA, 24–28 July 2000; Volume 3, pp. 1078–1080. [\[CrossRef\]](#)
14. Fusco, A.; Galdi, C.; Ricci, G.; Tesauro, M. Fitting a statistical model to SIR-C SAR images of the sea surface. *IEEE Trans. Aerosp. Electron. Syst.* **2004**, *40*, 1179–1190. [\[CrossRef\]](#)
15. Li, H.C.; Hong, W.; Wu, Y.R.; Fan, P.Z. On the Empirical-Statistical Modeling of SAR Images With Generalized Gamma Distribution. *IEEE J. Sel. Top. Signal Process.* **2011**, *5*, 386–397. [\[CrossRef\]](#)
16. Khan, S.; Guida, R. Application of Mellin-Kind Statistics to Polarimetric G Distribution for SAR Data. *IEEE Trans. Geosci. Remote Sens.* **2014**, *52*, 3513–3528. [\[CrossRef\]](#)
17. Sun, J.; Wang, X.; Yuan, X.; Zhang, Q.; Guan, C.; Babanin, A. The Dependence of Sea SAR Image Distribution Parameters on Surface Wave Characteristics. *Remote Sens.* **2018**, *10*, 1843. [\[CrossRef\]](#)
18. Lin, H.; Xu, Q.; Zheng, Q. An overview on SAR measurements of sea surface wind. *Prog. Nat. Sci.* **2008**, *18*, 913–919. [\[CrossRef\]](#)
19. Hersbach, H.; Stoffelen, A.; de Haan, S. An improved C-band scatterometer ocean geophysical model function: CMOD5. *J. Geophys. Res. Ocean.* **2007**, *112*, 1–18. [\[CrossRef\]](#)
20. Ren, L.; Yang, J.; Mouche, A.; Wang, H.; Wang, J.; Zheng, G.; Zhang, H. Preliminary Analysis of Chinese GF-3 SAR Quad-Polarization Measurements to Extract Winds in Each Polarization. *Remote Sens.* **2017**, *9*, 1215. [\[CrossRef\]](#)
21. Zanchetta, A.; Zecchetto, S. Wind direction retrieval from Sentinel-1 SAR images using ResNet. *Remote Sens. Environ.* **2021**, *253*, 112178. [\[CrossRef\]](#)
22. Zhang, B.; Perrie, W.; Vachon, P.W.; Li, X.; Pichel, W.G.; Guo, J.; He, Y. Ocean Vector Winds Retrieval From C-Band Fully Polarimetric SAR Measurements. *IEEE Trans. Geosci. Remote Sens.* **2012**, *50*, 4252–4261. [\[CrossRef\]](#)
23. Mouche, A.A.; Collard, F.; Chapron, B.; Dagestad, K.F.; Guitton, G.; Johannessen, J.A.; Kerbaol, V.; Hansen, M.W. On the Use of Doppler Shift for Sea Surface Wind Retrieval From SAR. *IEEE Trans. Geosci. Remote Sens.* **2012**, *50*, 2901–2909. [\[CrossRef\]](#)
24. Kerbaol, V.; Chapron, B.; Vachon, P.W. Analysis of ERS-1/2 synthetic aperture radar wave mode images. *J. Geophys. Res. Ocean.* **1998**, *103*, 7833–7846. [\[CrossRef\]](#)
25. Wang, C.; Mouche, A.; Tandeo, P.; Stopa, J.E.; Longépé, N.; Erhard, G.; Foster, R.C.; Vandemark, D.; Chapron, B. A labelled ocean SAR imagery dataset of ten geophysical phenomena from Sentinel-1 wave mode. *Geosci. Data J.* **2019**, *6*, 105–115. [\[CrossRef\]](#)
26. Melsheimer, C.; Alpers, W.; Gade, M. Simultaneous observations of rain cells over the ocean by the synthetic aperture radar aboard the ERS satellites and by surface-based weather radars. *J. Geophys. Res. Ocean.* **2001**, *106*, 4665–4677. [\[CrossRef\]](#)
27. Zhao, Y.; Longépé, N.; Mouche, A.; Husson, R. Automated Rain Detection by Dual-Polarization Sentinel-1 Data. *Remote Sens.* **2021**, *13*, 3155. [\[CrossRef\]](#)
28. Torres, R.; Snoeij, P.; Geudtner, D.; Bibby, D.; Davidson, M.; Attema, E.; Potin, P.; Rommen, B.; Floury, N.; Brown, M.; et al. GMES Sentinel-1 mission. *Remote Sens. Environ.* **2012**, *120*, 9–24. [\[CrossRef\]](#)
29. Stopa, J.E.; Sutherland, P.; Ardhuin, F. Strong and highly variable push of ocean waves on Southern Ocean sea ice. *Proc. Natl. Acad. Sci. USA* **2018**, *115*, 5861–5865. [\[CrossRef\]](#)
30. Dong, Y.; Liu, Y.; Hu, C.; MacDonald, I.R.; Lu, Y. Chronic oiling in global oceans. *Science* **2022**, *376*, 1300–1304. [\[CrossRef\]](#)
31. Wang, C.; Tandeo, P.; Mouche, A.; Stopa, J.E.; Gressani, V.; Longepe, N.; Vandemark, D.; Foster, R.C.; Chapron, B. Classification of the global Sentinel-1 SAR vignettes for ocean surface process studies. *Remote Sens. Environ.* **2019**, *234*, 111457. [\[CrossRef\]](#)
32. Eltoft, T.; Hogda, K. Non-Gaussian signal statistics in ocean SAR imagery. *IEEE Trans. Geosci. Remote Sens.* **1998**, *36*, 562–575. [\[CrossRef\]](#)
33. Buono, A.; Nunziata, F.; Migliaccio, M. Analysis of Full and Compact Polarimetric SAR Features Over the Sea Surface. *IEEE Geosci. Remote Sens. Lett.* **2016**, *13*, 1527–1531. [\[CrossRef\]](#)
34. Huang, X.; Zhang, B.; Perrie, W.; Lu, Y.; Wang, C. A novel deep learning method for marine oil spill detection from satellite synthetic aperture radar imagery. *Mar. Pollut. Bull.* **2022**, *179*, 113666. [\[CrossRef\]](#) [\[PubMed\]](#)